Discrete-element-method model for frictional fibers

Jérôme Crassous *

Université Rennes, CNRS, IPR (Institut de Physique de Rennes) - UMR 6251, F-35000 Rennes, France

(Received 20 April 2022; revised 14 November 2022; accepted 1 February 2023; published 22 February 2023)

We present a discrete-element-method algorithm for the simulation of elastic fibers in frictional contacts. The fibers are modeled as chains of cylindrical segments connected to each other by springs taking into account elongation, bending, and torsion forces. The frictional contacts between the cylinders are modeled using a Cundall and Strack model routinely used in granular material simulations. The physical scales for simulations, the determination and the tracking of contacts, and the algorithm are discussed. Tests on different situations involving few or many contact points are presented and compared to experiments or to theoretical predictions.

DOI: 10.1103/PhysRevE.107.025003

I. INTRODUCTION

The use of natural or artificial fibers allows one to design materials with original mechanical properties. At the nanometric or micrometric scales, carbon nanotubes [1] or polymer fibers [2] can be assembled into threads or networks. At the micrometer and millimeter scales, the frictional forces act with the elasticity of the fibers to produce a wide variety of materials. The fibers can just be deposited without any special preparation to form highly elastic media [3] such as cushions or nonwoven fabrics [4]. Textile fibers can be twisted to produce yarns [5–7], which are then assembled into cords [8], as well as woven [9] or knitted fabrics [9,10]. Cyclic mechanical stresses can form very compact natural structures [11] and birds also assemble fibers to build their nests [12,13]. The contacts between fibers play a fundamental role in describing the physics of knots, which is a subtle competition between tension and friction [14,15], as well as eventual bending of the fibers [16–19].

Several approaches have been proposed to numerically simulate these structures. One approach is to use finite-element algorithms to discretize the fibers [20]. This approach allows a complete solution of the elasticity equations in complex geometries such as nodes [18], but is only possible for systems with small numbers of contacts. Another approach is to model the fibers as connected spheres [21] or sphero-cylinders [22] and to use the discrete-element-method algorithm widely used for the study of granular materials. However, the periodic variations of diameter of such fiber may induce very specific physical properties as interlocked granular chains stiffening [23].

More realistic approaches are the simulations of fibers as discrete [24] or continuous [25,26] cylindrical elastic chains of circular cross sections. The noninterpenetration condition between fibers and surfaces, or between fibers, is then treated as constraints on the displacements. The introduction of frictional tangential forces in such model has been proposed using methods for finding forces that match the Coulomb conditions [25–27]. In those algorithms, the fibers are moved in order to find the positions of the surfaces that match the nonpenetration of fibers, with forces verifying the Coulomb condition. Those positions are found using an iterative procedure with proper regularization of Coulomb law to ensure the convergence towards one solution verifying the force balance. In the case where many frictional contacts are present, the problem becomes hyperstatic and the solution is not expected to be unique. This is a well-known situation in granular material [28] simulations, and the solutions selected by iterative algorithms are not well controlled [28] and presumably depend on the algorithm itself. Those drawbacks are, of course, of minimal importance in situations where the indeterminacy in contact forces is absent (hypo- or isostatic problem), such as in knots with few contacts [29], or if qualitative simulations are needed, as in the computer graphic community [30]. In explicit methods, the forces are obtained directly from the kinematic of the body in contacts. The selection of one solution of the Coulomb friction forces among many others is then ensured by the dynamics of the system. In counterpart, the explicit algorithm is usually slower.

Chains of cylinders with frictional contacts were first introduced in the discrete-element method by Chareyre *et al.* These authors used them for the study of the mechanical properties of granular materials reinforced with fibers [31,32], with geotextiles [33], and for the behavior of suspensions of frictional fibers in viscous flow [34].

This bibliography shows that the modeling of fibers in chains of discrete elements has been the subject of many studies, but scattered in different fields. Moreover, the ability of these different models to quantitatively reproduce the behavior of fibers systems with many frictional contacts has never been shown. Systems of fibers in frictional interactions are the object of a growing interest of physicists and mechanics. The object of this study is to propose to the community a simple discrete-element method, easily reproducible, and founded on the discrete-element-rod model, which includes frictional contacts and whose capacity to reproduce the behavior of various frictional fibers is clearly demonstrated.

*jerome.crassous@univ-rennes1.fr

 ©2023 American Physical Society

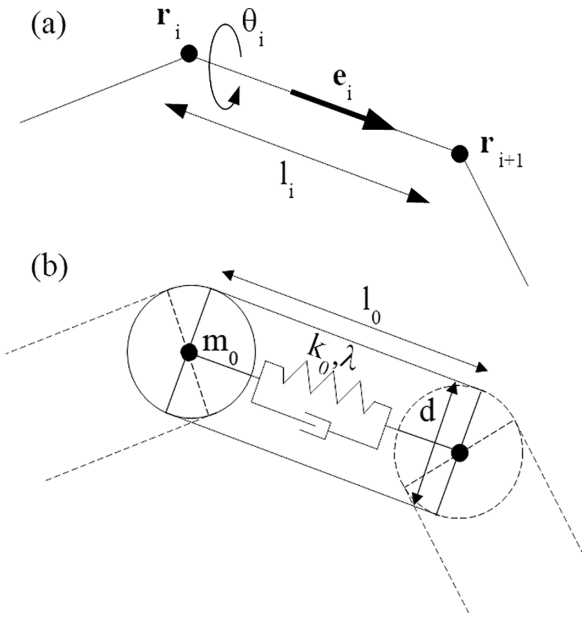

FIG. 1. (a) Ensemble of connected point forming the skeleton of the fiber. (b) Cylinders and spheres forming the shell of the fibers.

We will base the model on the theory of elastic chains as proposed by Bergou *et al.* [24]. We will keep a formulation with independent elastic constants of torsion, bending, and torsion, i.e., not linked by a cylindrical beam elasticity. This will allow one to simulate various systems, such as arbitrarily flexible wires. The contacts will be treated following an approach proposed by Chareyre *et al.* [31]. The ingredients of the modeling, as well as the calculations, will be presented in the simplest possible way so that this simulation can easily be reproduced by physicists from various fields.

The manuscript is organized in the following way. In Sec. II, we first describe the mechanical model of our fibers, including internal elastic forces and contact forces. The numerical resolution is then detailed in Sec. III, where we insist on points that are specific compared to discrete-element-method (DEM) simulations of frictional beads, i.e., the numerical scales that are used, the integration of displacement, and the search of neighbors. In Sec. IV, we illustrate this algorithm on various situations including static and dynamics, with few and many contacts.

II. MECHANICAL MODEL OF FIBERS IN CONTACT

A. Description of the fiber

Following [24], we model a fiber as an ensemble of N connected points [see Fig. 1(a)]. Let $\mathbf{r}_i$, with $0 \leqslant i \leqslant N-1$ be the position of the point, and $\mathbf{e}_i = (\mathbf{r}_{i+1} - \mathbf{r}_i)/\|\mathbf{r}_{i+1} - \mathbf{r}_i\|$, with $0 \leqslant i \leqslant N-2$ the unit vector joining two successive points. We note $l_i = \|\mathbf{r}_{i+1} - \mathbf{r}_i\|$. The segment joining two successive points is the generatrix of a cylinder of circular basis of diameter d. In addition, each point $\mathbf{r}_i$ is the center of a sphere of diameter d. So each fiber is a set of N spheres connected by $N-1$ cylindrical segments. A mass m_0 is assigned to each node of the string, and a moment of inertia J is assigned to each cylinder.

The kinematic of the deformation is the following. The different nodes of one fiber may translate, allowing the bending and the stretching of the fiber. The cylinders joining the different nodes remain straight cylinders and are not bent when the fiber is deformed. The rectilinear shape allows one to determine the contacts between fibers as contacts between cylinders. The cylinders may rotate around their axis, allowing the twist of the fibers. The kinematic of the chain is then determined by the set of N node positions $\mathbf{r}_i$, and $N-1$ cylinder rotations θ_i. To those degrees of freedom, we associate forces that act on nodes, and torques along the axis of cylinders. Any system of forces or torques, such as contact forces or elastic forces, acting on a cylinder will be decomposed as an axial torque and forces on nodes. This decomposition will be detailed below for elastic twist torques and contact forces.

B. Internal elastic forces

The internal elastic forces that we consider in the following are elongation, flexion, and twist forces. The elongational forces are modeled using springs of stiffness, k_0, with dashpots of damping λ. The equilibrium length of the spring is l_0, and the elongation force exerted by point $i+1$ on the mass located at $\mathbf{r}_i$ is

$$\mathbf{f}^{(e)}_{i+1;i} = [k_0\,(l_i - l_0) + \lambda\,\dot{l}_i]\mathbf{e}_i. \tag{1}$$

Each point i is submitted to forces from points $i-1$ and $i+1$ so that $\mathbf{f}^{(e)}_i = \mathbf{f}^{(e)}_{i+1;i} + \mathbf{f}^{(e)}_{i-1;i}$, except the first $i=0$ and last $i = N-1$ points.

The flexion forces acting on the point i are obtained from the elastic bending energy $E^{(b)} = \int_s (B/2)\,\kappa^2\,ds$, with B the bending stiffness of the fiber and κ the curvature. The bending energy of the discrete fiber is

$$E^{(b)} = \frac{B\,l_0}{2}\sum_{i=1}^{i=N-2}\kappa_i^2, \tag{2}$$

where κ_i is the curvature at node i, and the summation is extended to all nodes except ending ones. Writing the curvatures κ_i as function of nodes positions $\mathbf{r}_i$, the flexion force $\mathbf{f}^{(b)}_i = -(\partial E^{(b)}/\partial \mathbf{r}_i)$ acting on nodes i is (see the Appendix A1)

$$\mathbf{f}^{(b)}_i = -\frac{B}{l_0^3}[\mathbf{r}_{i-2} - 4\mathbf{r}_{i-1} + 6\mathbf{r}_i - 4\mathbf{r}_{i+1} + \mathbf{r}_{i+2}], \tag{3}$$

for $(N-3) \geqslant i \geqslant 2$. Expressions of the forces $\mathbf{f}^{(b)}_i$ for $i < 2$ and $i > (N-3)$ are given in the Appendix A1. The calculation supposes that the fibers are weakly extended and bent (see the Appendix A1).

The internal elastic torque is obtained from the twisting energy [24]: $E^{(t)} = \int_s (C/2)\,\tau^2\,ds$, with C the torsion modulus of the fiber and τ the twist of the fiber. The twist may be written as [35–37] $\tau = \tau_{\text{int}} + \tau_s$. The internal twist τ_{int} is the twist of the fiber if simply unbent, whereas τ_s is the torsion of the fiber center line. Writing the internal twist at node i as $(\theta_i - \theta_{i-1})/l_0$, and $\tau_{s,i}$ the torsion of the center line at node i, we obtain the twist energy of the discrete fiber as

$$E^{(t)} = \frac{C\,l_0}{2}\sum_{i=1}^{i=N-2}(\theta_i - \theta_{i-1} + l_0\,\tau_{s,i})^2. \tag{4}$$

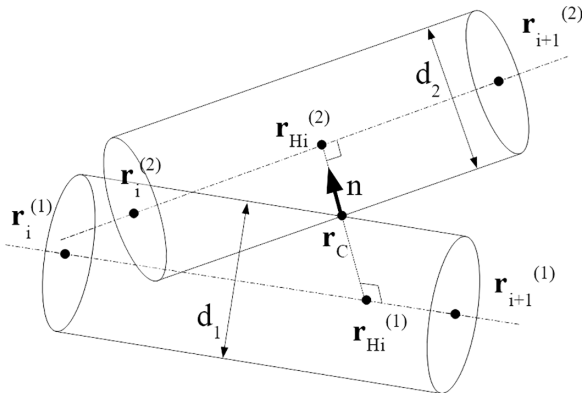

FIG. 2. Contact between two cylinders.

The twist moment acting on the segment joining nodes i and $i+1$ is obtained by differentiating (4) with respect to θ_i (see the Appendix, Sec. A 2):

$$\mathbf{m}_i^{(t)} = \frac{C}{l_0}[(\theta_{i+1} - \theta_i + l_0\,\tau_{s,i+1})\,\mathbf{e}_{i+1} - (\theta_i - \theta_{i-1} - l_0\,\tau_{s,i})\,\mathbf{e}_{i-1}]. \tag{5}$$

This elastic moment is split into one component $m_i^{(t)} = \mathbf{m}_i^{(t)} \cdot \mathbf{e}_i$ of the moment along the axis of the segment $(i, i+1)$, and into forces acting on nodes (see the Appendix, Sec. A 2).

C. Contact forces

Contact between fibers may occur between segments of cylinders or spheres belonging to identical or different fibers. Figure 2 shows the contact between two sections of cylinders. The contact point $\mathbf{r}_C(t)$ is located on the segment with ending points $\mathbf{r}_{H_i}^{(1)}$ and $\mathbf{r}_{H_i}^{(2)}$ on axis cylinders, which minimizes the distance between axes. This segment is unique if the axes are not parallel. The determination of this segment will be detailed in Sec. III C. Let $d(t) = \|\mathbf{r}_{H_i}^{(2)} - \mathbf{r}_{H_i}^{(1)}\|$ be this minimal distance and $\mathbf{n}(t)$ the normal unitary vector. We note $\delta(t) = (d_1 + d_2)/2 - d(t)$ to be the interpenetration of the two cylinders, and $\mathbf{r}_C(t) = \mathbf{r}_{H_i}^{(1)} + (r_1 - \delta/2)\,\mathbf{n}$ the contact point. We use the Cundall-Strack model for the contact force [38]. The normal contact force exerted by cylinder 1 on cylinder 2 is modeled as a spring-dashpot system,

$$\mathbf{f}_n^{(c)} = -[k_n\,\delta + \lambda_n\,\dot{\delta}]\mathbf{n}, \tag{6}$$

with k_n the contact stiffness between the cylinders and λ_n the contact damping. This contact law is a simplified version of the elastic contact force between two cylinders [39] which varies nonlinearly with the interpenetration $f_n^{(c)} \sim \delta^{3/2}$, and which depends on the angle between the cylinder axes. The tangential contact force is a Coulomb force,

$$\mathbf{f}_t^{(c)} = -\mathrm{Min}[k_t\,u_t; \mu k_n \delta]\,\frac{\mathbf{u}_t}{u_t}, \tag{7}$$

where k_t is the tangential stiffness, $\mathbf{u}_t$ the tangential displacement, and μ the microscopic friction coefficient. The tangential displacement $\mathbf{u}_t$ is initialized to 0 when the contact is first formed and evolves with time in the following way.

First, since the tangential displacement is expressed in the fixed frame, $\mathbf{u}_t$ is first rotated to take into account the rotation of the normal vector. Let $d\beta$ be the angle between the normal at times $t - dt$ and t: $\mathbf{n}(t - dt)$ and $\mathbf{n}(t)$, and $\mathbf{k} = [\mathbf{n}(t - dt) \times \mathbf{n}(t)]/|\mathbf{n}(t - dt) \times \mathbf{n}(t)|$ the axis rotation. We name $\mathbf{u}_t^{\mathrm{rot}}(t - dt)$ this rotated tangential displacement.

Then, the displacement is integrated as

$$\mathbf{u}_t(t) = \mathbf{u}_t^{\mathrm{rot}}(t - dt) + (\mathbf{v}^{(2)} - \mathbf{v}^{(1)})dt, \tag{8}$$

where $\mathbf{v}^{(1)}$ (and similar for $\mathbf{v}^{(2)}$) is the velocity of the point of the cylinder (1) coinciding with the contact point C. The velocity is $\mathbf{v}^{(1)} = \dot{\mathbf{r}}_i^{(1)} + \mathbf{\Omega}_i^{(1)} \times (\mathbf{r}_C - \mathbf{r}_i^{(1)})$, with $\mathbf{\Omega}_i^{(1)}$ the rotational velocity of the segment i of fiber 1. The rotation vector is separated into axial and nonaxial components as $\mathbf{\Omega}^{(1)} = \mathbf{\Omega}_\perp^{(1)} + \dot{\theta}_i\mathbf{e}_i$, where the nonaxial component is $\mathbf{\Omega}_{i,\perp}^{(1)} = \frac{1}{l_i}\mathbf{e}_i \times (\dot{\mathbf{r}}_{i+1}^{(1)} - \dot{\mathbf{r}}_i^{(1)})$.

Finally, the normal component $(\mathbf{u}_t \cdot \mathbf{n})\,\mathbf{n}$ is removed. If $k_t u_t > \mu k_n \delta$, then the tangential displacement is renormalized such that $u_t = \mu k_n \delta / k_t$.

The contact force $\mathbf{f}^{(c)}$ is then expressed as a system of forces $\mathbf{f}_i^{(c)}$ and $\mathbf{f}_{i+1}^{(c)}$ applied on nodes i and $i+1$, and a moment $m_i\mathbf{e}_i$ acting on the cylinder connecting those nodes. The conservation of the resultant and of the moment of contact force implies that

$$\mathbf{f}_i^{(c)} + \mathbf{f}_{i+1}^{(c)} = \mathbf{f}^{(c)}, \tag{9a}$$

$$(\mathbf{r}_{i+1} - \mathbf{r}_i) \times \mathbf{f}_{i+1} + m_i\mathbf{e}_i = (\mathbf{r}_C - \mathbf{r}_i) \times \mathbf{f}^{(c)}. \tag{9b}$$

A possible choice for forces and moment is (see the Appendix, Sec. A 3)

$$m_i^{(c)} = [(\mathbf{r}_C - \mathbf{r}_i) \times \mathbf{f}^{(c)})] \cdot \mathbf{e}_i, \tag{10a}$$

$$\mathbf{f}_i^{(c)} = (1 - s_i)\mathbf{f}^{(c)} + \frac{R}{l_i}(\mathbf{f}^{(c)} \cdot \mathbf{e}_i)\mathbf{n}, \tag{10b}$$

$$\mathbf{f}_{i+1}^{(c)} = s_i\mathbf{f}^{(c)} - \frac{R}{l_i}(\mathbf{f}^{(c)} \cdot \mathbf{e}_i)\mathbf{n}. \tag{10c}$$

It should be noticed that (9) does not set all the components of $\mathbf{f}_i^{(c)}$ and $\mathbf{f}_{i+1}^{(c)}$, and that supplementary conditions expressed in the Appendix, Sec. A 3, must be added to obtain (10).

If the contact between two fibers involves one cylindrical segment of the fiber and one sphere, or two spheres, the contact point is calculated according to the type of the surfaces in contact. The translation velocity of the sphere is the velocity of the node. The rotation velocity of the sphere at node i is the rotation velocity of the cylinder joining nodes i with $i+1$.

D. Miscellaneous forces

In addition, miscellaneous extra forces may be added. A global viscous damping force $\mathbf{f}_i^{(v)} = -\lambda_v\,\dot{\mathbf{r}}_i$ may be added. It is useful to damp transverse motion of fibers. Indeed, our mechanical model of fiber does not include any dissipation for motion perpendicular to the fiber axis if there are no contacts. Volumetric forces such as gravity forces $\mathbf{f}_i^{(g)} = m_0\,\mathbf{g}$, with $\mathbf{g}$ the gravity field, may also be added. Other external forces may be applied to fibers such as pretension at the ends of the fibers.

III. NUMERICAL IMPLEMENTATION

A. Integration of equation of motions

The dynamical equations of motions are written as

$$M_0\,\ddot{\mathbf{r}}_i = \mathbf{f}_i^{(e)} + \mathbf{f}_i^{(b)} + \mathbf{f}_i^{(c)} + \mathbf{f}_i^{(v)} + \mathbf{f}_i^{(g)}, \tag{11a}$$

$$J_z\,\ddot{\theta}_i = m_i^{(t)} + m_i^{(c)}. \tag{11b}$$

The second equation describes the rotation of the cylinder segment around its axis. We did not consider in Eq. (11b) any elastic torque due to torsion of the fiber, and the fiber is free to rotate around node $\mathbf{r}_i$. The dynamical equations are integrated using a standard second-order Verlet algorithm [40].

B. Physical parameters for simulations

1. Physical scales

We first define mass, length, and stiffness scale for the simulation. The mass scale m_0 is the point mass of the nodes, the length scale l_0 is the equilibrium length of each segment, and the stiffness scale k_0 is the elongation stiffness of the spring. If all the fibers do not have identical physical properties, those scales are chosen from the fibers of the smallest radius. For every physical quantity x, with a physical scale x_0, we note the nondimensional quantity as $x^* = x/x_0$.

The timescale is $t_0 = (m_0/k_0)^{1/2}$. For fibers of diameters $r = d/2$ made of an elastic material (Young modulus E, Poisson coefficient ν) of density ρ, we have $k_0 = E\pi r^2/l_0$, $m_0 = \rho\pi r^2 l_0$, and then $t_0 = l_0\,(\rho/E)^{1/2}$. The timescale t_0 is then the time of propagation of the compression waves through one segment of the fiber. The force scale $f_0 = k_0\,l_0 = E\pi r^2$ is the force that extends a hypothetical perfectly elastic fiber by 100%.

2. Elastic forces and damping

When submitted to a traction force f, the relative expansion of the fibers is $f/f_0 = f^*$. It follows that if we want to stay in the limit of small extension, we should keep $f^* \ll 1$. In practice, the simulations are done with $f^* \sim 10^{-5}$–10^{-3}. It should be noted that if f^* is too small, the propagation of transverse waves is very slow when no bending forces are present. Indeed, the velocity of transverse wave v_t in a string of linear density ρ_l under a tension f is $v_t = (f/\rho_l)^{1/2}$. With $\rho_l = m_0/l_0$, we have $\rho_l^* = 1$ and the nondimensional speed of the transverse wave is $v_t^* = (f^*/\rho_l^*)^{1/2} = (f^*)^{1/2}$ when no bending stiffness is present.

The nondimensional bending stiffness is $B^* = B/k_0 l_0^3$. For an elastic fiber as consider in Sec. III B 1, we have $B = E\pi r^4/4$, and then $B^* = (r^*)^2/4$. Similarly, the nondimensional torsional modulus is $C^* = C/k_0 l_0^3$. For an elastic fiber of radius r, we have $C = E\pi r^4/2(1+\nu)$, and then $C^* = (r^*)^2/2(1+\nu)$.

The longitudinal damping λ is chosen to avoid compression waves that travel continuously through the fibers, needing a very long time to return to equilibrium. We take $\lambda \sim (k_0 m_0)^{1/2}$, and then $\lambda^* \sim 1$ for this.

3. Contact force

The value of the contact stiffness is fixed from a linearization of the Hertzian contact between two elastic cylinders. If two cylinders of radius r with perpendicular axes are in contact, the problem is equivalent to the the contact between a sphere of radius r and a plane, and the normal force is $f_n = (4/3)\,E_{\text{eff}}\,r^{1/2}\,\delta^{3/2}$, with $E_{\text{eff}} = E/(1-\nu^2)$, and ν being the Poisson ratio of the material. To do the linearization, we arbitrarily set that the elastic energy of the Hertzian contact, $\sim E_{\text{eff}}\,r^{1/2}\,\delta^{5/2}$, is equal to the elastic energy $k_n\delta^2/2$ of the spring for a normal force f which is of the order of the traction force that we applied on the fibers. Dropping the numerical factor of the order of 1, we obtain $k_n = E^{2/3}\,f^{1/3}\,r^{1/3}$. The nondimensional stiffness may then be obtained as

$$k_n^* = \frac{(f^*)^{1/3}}{r^*}, \tag{12}$$

where we again dropped the constant term. f^* is the typical nondimensional force (i.e., the nondimensional traction applied to the fibers). This value of k_n^* is a reasonable choice for modeling the contact, but evidently different values may be set. In practice, since the tension is of the order of $f^* \sim 10^{-5}$–10^{-3}, and the typical radius is $r^* \sim 10^{-1}$, we have $k_n^* \sim 1$. For the sake of simplicity, the tangential stiffness is taken as $k_t^* = k_n^*$.

Some damping of the normal force, λ_n, may be introduced. We took $\lambda_n^* \sim 1$ for the rapid relaxation of the oscillating motion of the contact.

4. Timescale for simulation

The time step dt for the simulation is chosen such that the dynamic of the length relaxation and of the contact establishment is correctly described. The length of the segment relaxes on a timescale $\sim(m_0/k_0)^{1/2} = t_0$, whereas the timescale for a contact to establish is $\sim(m_0/k_n)^{1/2} = t_0\,(k_0/k_n)^{1/2}$. The time step is chosen as $dt = \text{Min}[t_0; t_0\,(k_0/k_n)^{1/2}]/10$, leading to

$$dt^* = \frac{1}{10}\,\text{Min}[1; (k_n^*)^{-1/2}], \tag{13}$$

such that both relaxations occur on at least 10 time steps. In practice, since $k_n^* \sim 1$, we take $dt^* = 0.1$. For a given set of parameters, it is checked that results are unchanged if time steps are divided by a factor 2.

C. Computation of contact points

The discrete-element method is mainly used in assemblies of spherical particles. Due to the anisotropic shape of the segments, our algorithm for the determination of the contact points has some particularities compared to the sphere-sphere contact that we discuss in this section.

1. Distance between fibers

The distance between fibers is calculated in the following way. We first consider a segment as a set composed of a sphere and a part of a cylinder, as shown in Fig. 3(a). We first calculate the distance between the two parts of the cylinders following the method described in the Appendix, Sec. A 4. If contact does not occur along the two cylinders, contact between spheres and cylinders are searched, and finally between the two spheres. The hull of the fiber is therefore composed of the external surface of the cylinders and of the spheres,

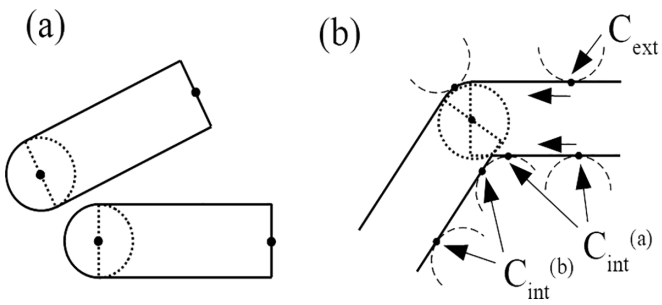

FIG. 3. (a) Two -dimensional (2D) view of two sets, composed of one sphere and one cylinder. (b) Motions of external C_{ext} and internal C_{int} contact points at the junction between two cylinders.

as shown in Fig. 3(b). The start and the end of the fibers are finished by spheres.

2. *Integration of displacement of contact point*

The contact point is followed continuously during the motion of the fibers. This may be done easily as long as the contact point between one segment and one fiber is unique as, for example, the contact point C_{ext} in Fig. 3(b). In this case, the displacement of the contact point is continuously integrated along the motion. In some cases, two contact points may exist simultaneously as the two points as, for example, the contact points $C_{\text{int}}^{(a)}$ and $C_{\text{int}}^{(b)}$ in Fig. 3(b). When the contact at point $C_{\text{int}}^{(b)}$ occurs, its tangential displacement is initially set to 0 (as every new contact), and this lowers the tangential force. Since the fibers weakly bend with $r \ll l_0$, we expect that the number of such contacts is very small compared to the total number of contacts, producing very negligible errors. A possible refinement may be to interpolate the two contact points as a single one, allowing a continuous integration of displacement.

3. *Neighbor search method*

The search for contacts between discrete objects can significantly increase the computation time of DEM algorithms. In our case, the algorithm for measuring the distance between cylinders is slightly more complex than for spheres, further increasing the computation time of the collisions. Several strategies are possible to significantly improve the computation time of the collisions. They are based on the use of a neighbor list (Verlet list) or on the partition of the system in boxes (linked cell method). Here we discuss the problem arising when using strongly anisotropic objects. In the linked cell method, the particles are assigned in cells, and the list of particles is each cell is updated periodically. The collisions are searched only for particles within the same or the neighboring cells. This strategy is very effective for approximately monodisperse spheres. In the case of polydisperse spheres, the size of the cell must be a multiple of the size of the largest particles, so that the number of particles per box increases. As a consequence, the computation time grows rapidly with the polydispersity, as shown by Luding *et al.* [41]. The problem is very similar for strongly anisotropic particles such as fibers or segments of fibers. Figure 4(a) shows an assembly of fibers with segments of size l_0. If collisions between segments are

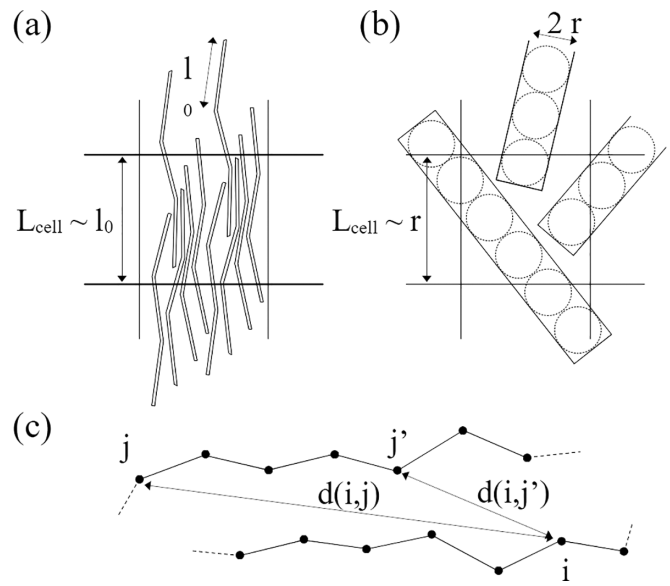

FIG. 4. Two possible choices for the size of the cells into which collisions between fibers may be searched: (a) size of the cell scales as the length of segments, (b) size of the cell scales as the radius of segments. (c) Simplification arising from the fact that the segments belonging to each fiber are connected.

searched within one or more neighboring cells, the size of the cell should be $\sim 2\,l_0$. For segments of section $\sim 4\,r^2$, the number of segments in each cell is $\sim 2\,(l_0/r)^2$ for a dense 3D system. Since $l_0/r \gg 1$, sorting particles in a cell of size $\sim l_0$ is not efficient. A more convenient way to define the cell may be considered. It consists, as shown in Fig. 4(b), of replacing segments by fictitious spheres of radius r inside each segment of length l_0, and considering cells of size $\sim 4\,r$. In this case, for a system of N_f fibers of N segments each, the total numbers of fictitious spheres is $\sim N_f N(l_0/2r)$. However, those two methods do not use the fact that different segments of one fiber are linked together. Taking advantage of this knowledge may significantly speed up the search of neighboring. Figure 4(c) shows two fibers, and we search the contact between segment i of fiber 1 with fiber 2 by increasing j. For a segment j, we calculate the distance $d(i, j)$. If this distance is larger than $2r$, there is no contact and we are sure that there is no contact between the two fibers for $|j' - j| \leqslant d(i, j) - 2r$. So the next segment where we need to search the contact verifies $j' > j + d(i, j) - 2r$.

The optimal strategy to find contacts is expected to be dependent on the type of fiber being studied. In the case of fibers with numerous segments, taking advantage of the constraint that the segments are linked, as depicted in Fig. 4(c), is presumably better. In contrast, in the case of an assembly of very short fibers, such as a packing of one-segment needles, the use of the cell, as in Fig. 4(b), should be preferred. Further study of such optimization is outside the scope of this study.

IV. ILLUSTRATION EXPERIMENTS

The program has been tested on various simple geometries in order to check the consistency with the theory, verify the numerical stability of the algorithm, and test the numerical

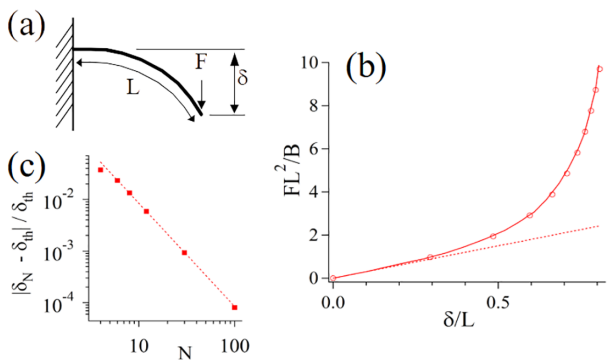

FIG. 5. Force applied to a beam as a function of its deflection. (a) Geometry. (b) Symbols: simulation results. Solid line: theoretical solution. Dashed line: force in the small deflection limit $FL^2/B = 3\delta/L$. (c) Convergence: δ_N is the end deflection for a beam with N nodes [$(N-1)$ cylinders] and δ_{th} is the theoretical deflection. Applied force is $FL^2/B = 10$. Symbols are the relative error and the dashed line is a N^{-2} decay.

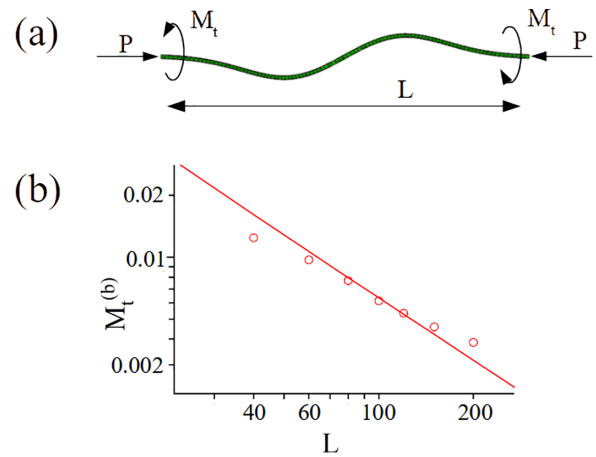

FIG. 6. Buckling of an elastic rod. (a) Geometry. (b) Torque applied at ends at the torsional buckling threshold as a function of the rod length. Symbol: simulation results with $P = 0$. Line: $M_t^{(b)} = 2\pi B/L$.

precision. Those configurations were the rolling or sliding of a cylinder on an inclined plane, the velocity of transverse waves of a string, the static flexion of a fiber loaded at extremity by a point force, and the catenary shape of a massive string under gravity. We present, in the following, four more complex situations. If not otherwise specified, the simulation parameters are the time step $dt^* = 0.1$, internal damping $\lambda^* = 2.8$, contact stiffness $k_n^* = k_t^* = 1$, contact damping $\lambda_n^* = 1$, global viscous damping $\lambda_v^* = 0.001$, and inertia momentum $J^* = m^* r^{*2}/2$ (homogeneous cylinder).

A. Elastic rods without contacts

The elastic rod model has already been tested in miscellaneous situations that do not involve frictional contacts [24]. The test examples presented here are just for checking the approximations used in Secs. II B and V.

The first example is the deformation of a clamped elastic rod ($N = 100$, $B^* = 0.1$) submitted to a point force applied at one end [see Fig. 5(a)]. The clamping is imposed by fixing the first and second nodes of the rod. The free rod length L is then the number of cylinders minus one, $N - 1$: $L = N - 2 = 98$. Results for different values of the applied forces are shown in Fig. 5(b). Those results may be compared to the deflection of an nonextensible rod. At small deflections $\delta \ll L$, $FL^2/B \simeq 3\delta/L$. At large deflections, $\delta \sim L$ simulations agree well with the analytical solution of Bisshopp *et al.* [42]. Simulations with beams made with different N show that the solution obtained with the discrete beam converges towards an analytical solution as $\sim N^{-2}$ [see Fig. 5(c)]. It may be noticed that since the maximum force applied in those simulations are of the order of $F \sim 10\,B/L^2$, the maximum nondimensional force $F^* \sim 10^{-4} << 1$, so that the beam stretching is negligible.

The second example is the buckling of a rod submitted to a compression and applied torque at its ends [see Fig. 6(a)]. A numeric rod ($B^* = 0.1$) is submitted to a torque M_t at its ends. The displacement of the ends perpendicularly to the axis of the rod is blocked, and no compression forces P are applied. The torque is slowly increased until buckling of the beam occurs. The buckling threshold is determined by measuring the displacement of the ends along the axis of the rod. Those displacements are initially negligible and suddenly increase as buckling occurs. Figure 6(b) shows the buckling torque $M_t^{(b)}$ as a function of the rod length. Stability analysis of the twisted rods leads to [43] $M_t^{(b)} = 2\pi B/L$. As shown in Fig. 6(b), the numerical results are in correct agreement with this theoretical law.

B. Static without flexion: Capstan

We simulate the tension along a string which is rolled up around a cylinder. For this, we prepare an infinitely flexible spring ($B^* = 0$, $N = 200$, $r^* = 0.1$) which makes five turns around a cylinder ($R^* = 5$). The cylinder had a huge mass and moment of inertia to prevent any motion. The friction coefficient is $\mu = 0.2$. We first apply an equal tension $T_1^* = T_2^* = 0.01$, with opposite directions, to the two ends of the string. We let the system reach equilibrium. Then, we slowly decrease T_2^* while keeping $T_1^* = 0.01$. For a threshold value of T_2^*, the sliding of the string occurs. We measure the tension in the string using (1) at the onset of sliding. Figure 7 shows the decrease of the tension T^* along the string as a function of $\theta = (s^* - s_0^*)/(R^* + r^*)$, with s^* the abscissa along the curve and s_0^* the abscissa of the first contact point. The solution of the capstan problem with a finite thickness rod predicts that [44] $T^*/T_1^* = \exp(-\mu\,\theta)$, which is the observed behavior in Fig. 7. The measured decay is $\mu = 0.198$, in agreement with the imposed value $\mu = 0.2$.

C. Static with flexion: Elastic knots

We consider the mechanical response of an elastic rod with an open knot. An elastic fiber of length L, with a circular section of radius r and bending modulus B, is bent in an open trefoil knot (3_1). We then apply a tension T to the ends of the fibers. This experimental situation has been addressed by Audoly *et al.* [16,17]. When the tension is weak, the loop radius R is very large compared to r. In this limit, the authors

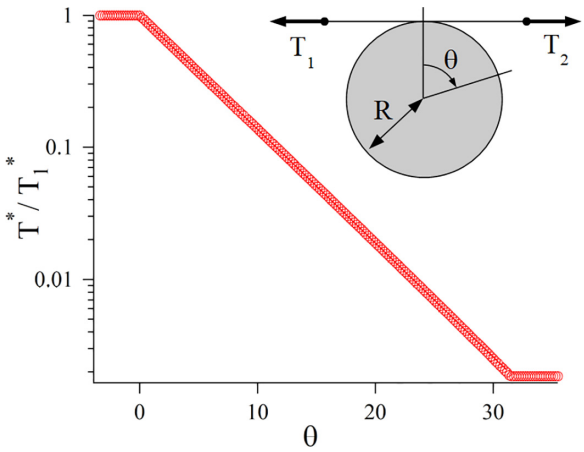

FIG. 7. Tension in a rolled string around a cylinder: T^* is the tension in the string and θ is the rolling angle. Circles are symbol; solid line is an exponential fit. See text for simulation parameters. Inset: Schematic of the experiment.

found analytical solutions for the shape of the knot, both in the frictionless case and for weak friction $\mu \ll 1$. This knot has been simulated very recently by Choi *et al.* using a discrete rod model with an implicit solver for the contact force [29].

We simulate numerically such knot by considering a flexible spring $r^* = 0.1$, $B^* = (r^*)^2/4 = 2.5\times10^{-3}$, $N = 500$, $\lambda_v^* = 4\times10^{-4}$, as shown in Fig. 8(a). We first knot the fiber by setting $\mu = 0$ and applying a tension $\pm T^*\mathbf{e}_z$ at the ends. After this preparation stage, we set μ to its actual value, and

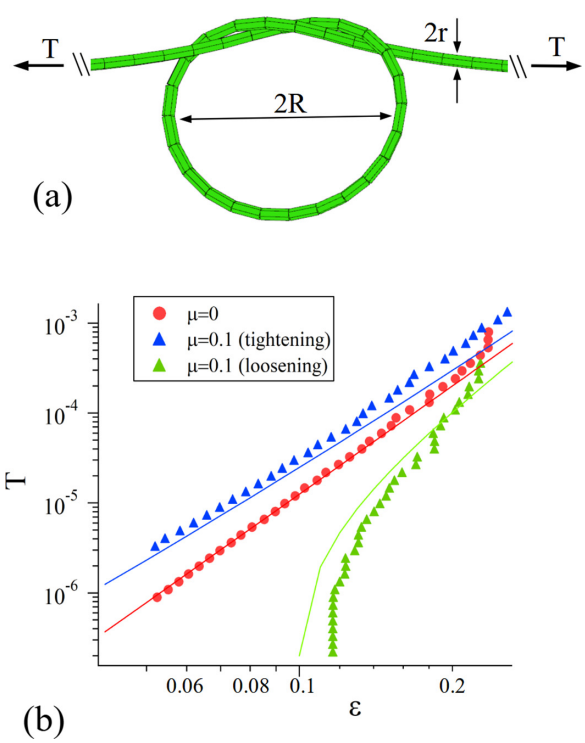

FIG. 8. (a) Snapshot of a (3_1) knot. For clarity, an illustration is made with $r^* = 0.2$. (b) Tension as a function of $\varepsilon = \sqrt{r/R}$ for frictionless and frictional strings. Symbols are numerical data, and lines are theoretical expressions given by Eq. (14).

we increase or decrease T^* depending on whether we tighten or loosen the knot. When the knot begins to move, we measure the radius of the curvature of the loop as $R = \langle \|d\mathbf{t}_i/ds\|^{-1}\rangle$, where $d\mathbf{t}_i/ds = \mathbf{e}_{i+1} - \mathbf{e}_i$ is the derivative of the tangent vector, and the average $\langle\,\rangle$ is over all segments in the loop which are at a distance of at least one segment from any contact point. Following [16,17], we introduce $\varepsilon = \sqrt{r/R}$. Figure 8(b) shows the tension T^* as a function of ε for frictionless ($\mu = 0$) and frictional ($\mu = 0.1$) loosening and opening of the knots. The analytical solutions in the limits $\varepsilon \ll 1$ and $\mu \ll 1$ are [16,17]

$$\frac{Tr^2}{B} = \frac{\varepsilon^4}{2} \pm \mu\sigma\varepsilon^3, \tag{14}$$

where the sign $\pm$ depends on whether the knot is tightened (+) or loosened (−), and σ is a numerical constant which is $\sigma \simeq 0.492$ for the trefoil knot. As shown in Fig. 8(b), the numerical data agree correctly with the analytical one. In the frictionless case, we may observe deviations from the scaling $T \sim \varepsilon^4$ when $\varepsilon \gtrsim 0.15$. Two possible sources of the deviations may be identified. First, Eq. (14) is obtained in the limit $\varepsilon \ll 1$, and deviations may arise from high-order ε terms in Eq. (14). Second, for $\varepsilon \gtrsim 0.15$, we have $R^* = R/l_0 = r^*/\varepsilon^2 \sim 4$, so that the discretization of the loop may then be an issue. The discrete nature of the rod may be clearly identified on numerical data from $\mu = 0.1$ loosening, where some steps in ε are visible. For the frictional case, the model (14) slightly underestimates the role of friction compared to the numerical simulations. It may be due to some departure from the hypothesis $\mu \ll 1$ which is used to obtain (14).

D. Impact: Falling chain

We consider the dynamics of the impact of a metallic chain on a cylindrical obstacle. We restrict this analysis to a qualitative analysis. A metallic chain (length $L = 190$ mm, mass $m = 8.5$ g) is held at its extremities by hands. The chain is released and its fall is recorded with a fast camera operating at 200 fps. Figure 9(a) show some snapshots of the impact. The chain is simulated as a infinitely flexible spring $B^* = 0$. We set the length scale to $l_0 = 2$ mm, and $N = 95$, so that $L = N\,l_0$. The choice of the timescales may be done in the following way. We want to simulate a nonextensible chain, so we require that the nondimensional typical force is $\ll 1$. The gravity force is $F_g = Nm_0g$, with m_0 the mass scale of one segment and g the gravity. The nondimensional gravity force is then $F_g^* = F_g/k_0l_0 = Ng/l_0t_0^{-2} = Ng^*$. We take $g^* = 4.9\times10^{-5}$ so that $N\,g^* \simeq 5\times10^{-3} \ll 1$. This sets the timescale $t_0 = 0.1$ ms. It should be noted that in the limit of a nonextensible chain, the mass scale does not need to be specified. Other parameters are $dt^* = 0.1$, $R^* = 5$, $r^* = 0.1$, $\mu = 0.1$, $k_n^* = k_t^* = 1$. Figure 9(b) shows the results of the simulations which qualitatively agree with the experiments. We may remark that the behavior of the experimental chain is not symmetric in compression and in extension (nearly infinite stiffness in extension, zero stiffness in compression), whereas the numerical chain is symmetric (same stiffness in compression and in extension). However, in the impact experiment, the chain is always in tension and the lack of symmetry does not have importance.

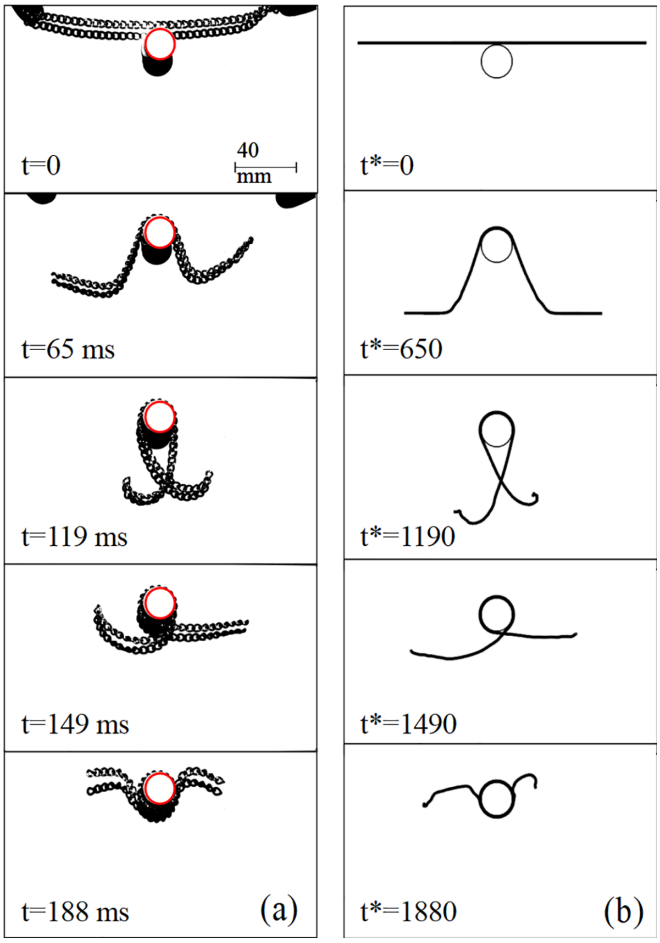

FIG. 9. (a) Experimental snapshots of the impact of a metallic chain on a fixed perpendicular cylinder of radius $R = 10$ mm. The perimeter of the cylinder is underlined in red. Time $t = 0$ is defined as the first contact time. Chain length $L = 190$ mm, mass $m = 8.5$ g. (b) Simulated impact. See text for physical parameters of the simulation.

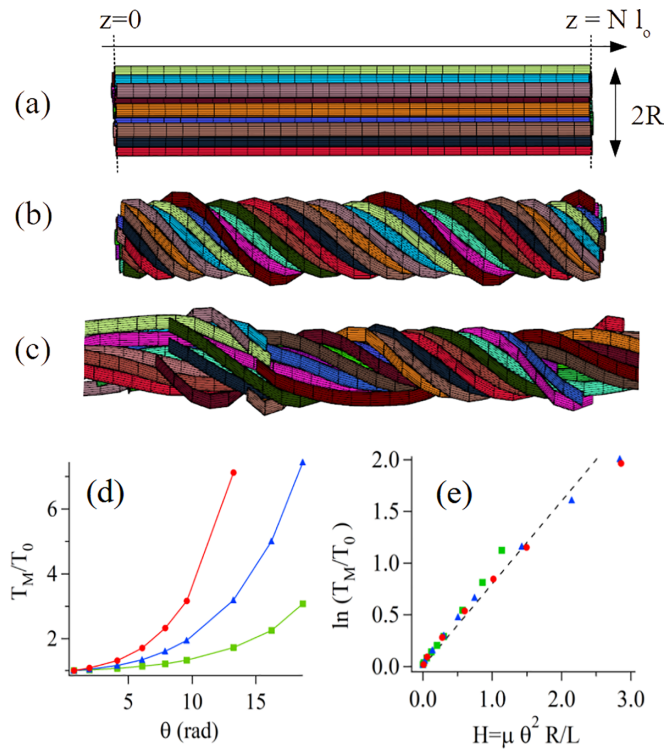

FIG. 10. (a) Assembly of initially straight fibers. (b) Thread of fiber after a torque is applied at the ends. (c) Separation of the fibers due to applied forces. (d) Force ratio necessary to separate the slivers as a function of the twist angles. Red disks: $\mu = 1$; blue triangles: $\mu = 0.5$; green squares: $\mu = 0.2$. Lines are for guidelines. (e) Same data as (d) plotted as a function of $\mathcal{H} = \mu\theta^2 R/L$. Dotted line is $0.75\,\mu\theta^2 R/L$. Simulation parameters are $N_f = 20$, $N = 30$, $r^* = 0.1$, $B^* = 0$. For clarity, (a)–(c) are enlarged by a factor of 6 perpendicularly to the z axis.

E. Multiple fibers: A yarn model

In a recent study, Seguin *et al.* considered the situation of a staple yarn made of twisted totally flexible fibers [7]. We present in this section some numerical details about this simulation. The yarn is made of an assembly of N_f identical fibers of N segments initially parallel to an axis z [see Fig. 10(a)]. Their positions $(x_i; y_i)$ in the plane perpendicular to the z axis, with $1 \leqslant i \leqslant N_f$, are the positions of a packing of disks in 2D obtained from a separate simulation.

In a first phase of the simulation, the fibers are twisted. The fibers are submitted to a tension $T^* = 10^{-4}$ along z, applied at both ends. A torque $C^*\mathbf{e}_z$ is applied to both ends of the assembly of fibers. For this, each fiber i with $1 \leqslant i \leqslant N_f$ is submitted at both ends $j = 0$ and $j = N$ to an external shear force,

$$\tau_i(j) = \pm\frac{C^*}{\sum_i r_i^2(j)}[\mathbf{e}_z \times \mathbf{r}_i(j)], \tag{15}$$

where the sign is $-$ for $j = 0$, and $+$ for $j = N$ ends. The torque is gradually increased until it reaches its target value and the shear forces are updated at each time step. Under the action of this torque, the fibers twist and becomes approximately helicoidal, as shown in Fig. 10(b). During this preparation, the friction coefficient is set to a low value, $\mu = 0.05$. This is important in order to obtain a regular pitch along the thread. Indeed, since the yarn is twisted by the application of torques at the ends, the presence of an important friction between fibers has the effect of concentrating the twist near the ends, with a central zone of low twist. This behavior is also observed experimentally [7] if the twist is not homogenized along the yarn. The duration of this preparation stage is $t^* = 5\times10^5$, and the total twist θ is measured at the end of this phase.

In a second phase, the fibers are separated. The friction is first set at its target value. The fibers are randomly partitioned in two sets: up and down. The tension of the up-fibers is multiplied by a factor $f > 1$ at the up-extremities: $T_{\rm up}(j = 0) = T^*$ and $T_{\rm up}(j = N) = f\,T^*$. Symmetrically, $T_{\rm down}(j = 0) = f\,T^*$ and $T_{\rm down}(j = N) = T^*$. The factor is $f = 1$ at the beginning of the separating stage and is increased at a fixed rate $(\Delta f/\Delta t^*) = 2\times10^{-6}$. During this phase, the torque is kept constant. The difference between the average positions of the up and down fibers is measured. This difference stays constant, until a threshold value of f where the two slivers

of fiber separate [see Fig. 10(c)]. A mechanical model of this problem developed in [7] shows that the force necessary to separate the two slivers is $\ln(1+f) \simeq 0.75\,\mu\theta^2 R/L$, which is the behavior that is observed in Fig. 10(e).

V. CONCLUSION

We have described a discrete-element mechanics algorithm for the simulation of flexible and frictional fibers. This algorithm is similar to the DEM-type algorithms widely used for the study of granular materials. The difference arises from the type of surfaces in contact (cylinders and not spheres) and from the elastic forces between the cylinders which are connected to form a fiber. The algorithm has been tested on various configurations that can be compared to experiments or to theoretical models.

The assumptions and approximations used to design this algorithm are quite limited. The low bending assumption is not very compelling for many applications, but could eventually be minimized by a finer discretization of the fiber. The simplification of the Hertzian elastic contact law between the cylindrical segments by a linear spring has probably a very small impact on the modeling of real systems. An extension to nonlinear contact laws should not be a problem. Finally, the discretization of the fiber generates a discontinuity of the displacement for some contact points at the passage between successive segments of a fiber. *A priori*, the number of such jumps is negligible compared to the total number of contacts for thin and weakly bent fibers, and this should not be an issue for simulations of real systems.

The main difference between this algorithm and those previously described to simulate elastic fibers lies in the level of simplification of the mechanical problem. Simulations of fibers with finite-element algorithms are certainly of high accuracy, but can only simulate small systems. Implicit algorithms are probably faster, but the indetermination of forces in multicontact cases is not resolved by the dynamics of the system. The use of a DEM algorithm is a compromise that allows one to consider relatively complex assemblies of fibers and that correctly handles the multiplicity of equilibrium solutions.

The potential applications of this algorithm are obviously multiple. The study of complex knots between fibers of ropes, with or without bending energy, is possible. The mechanical response of fiber clusters in nests, cushions, or in rigid needle stacks is also possible. For these studies, the contact search should be optimized according to the aspect ratio of the fibers and the geometry of the packing. The simulation of knitted or woven fabrics can also be considered. For this, large systems can be simulated, but the introduction of periodic boundary conditions should be more suitable. Finally, systems mixing fibers and grains for the study of soils reinforced by fibers or roots are also possible applications of this work.

ACKNOWLEDGMENT

The author would like to thank Antoine Seguin and Sean McNamara for discussions and careful reading of the manuscript, and Laurent Courbin for his help in experiments on falling chains.

APPENDIX

1. Flexion forces

The curvature κ_i at a node $N-2 \geqslant i \geqslant 1$ is first expressed as a function of the positions of nodes $\mathbf{r}_{i-1}$, $\mathbf{r}_i$ and $\mathbf{r}_{i+1}$. The radius $R_i = 1/\kappa_i$ of the circle joining those three points may be expressed as a function of the surface S_i and the perimeter p_i of the triangle with vertices $(\mathbf{r}_{i-1}, \mathbf{r}_i, \mathbf{r}_{i+1})$ using the Heron formula. After elementary calculus, we obtain

$$\kappa_i^2 = 4\,\frac{\mathbf{l}_{i-1}^2\mathbf{l}_i^2 - (\mathbf{l}_{i-1}\cdot\mathbf{l}_i)^2}{\mathbf{l}_{i-1}^2\,\mathbf{l}_i^2\,(\mathbf{l}_{i-1}+\mathbf{l}_i)^2}, \tag{A1}$$

where we noted $\mathbf{l}_i = \mathbf{r}_i - \mathbf{r}_{i-1}$. The bending energy is

$$E^{(b)} = \frac{B\,l_0}{2}\sum_{i=1}^{i=N-2}\kappa_i^2. \tag{A2}$$

The flexion force is then

$$\mathbf{f}_i^{(b)} = \frac{B\,l_0}{2}\frac{\partial}{\partial\mathbf{r}_i}\left[\sum_{i'=1}^{i'=N-2}\kappa_{i'}^2\right]. \tag{A3}$$

First, we notice that for weakly bending fibers, $\mathbf{l}_i \simeq \mathbf{l}_{i-1}$, and for weakly extended fibers, $l_i \simeq l_0$. Then, the denominator of (A1) is $\simeq 4\,l_0^6$,

$$\frac{\partial\kappa_{i'}^2}{\partial\mathbf{r}_i} \simeq \frac{1}{l_0^6}\frac{\partial}{\partial\mathbf{r}_i}\left[\mathbf{l}_{i'-1}^2\mathbf{l}_{i'}^2 - (\mathbf{l}_{i'-1}\cdot\mathbf{l}_{i'})^2\right]. \tag{A4}$$

Using $\mathbf{l}_i = \mathbf{r}_i - \mathbf{r}_{i-1}$, we obtain

$$\frac{\partial\kappa_{i-1}^2}{\partial\mathbf{r}_i} \simeq \frac{1}{l_0^4}[2(\mathbf{l}_{i-1} - \mathbf{l}_{i-2})], \tag{A5a}$$

$$\frac{\partial\kappa_i^2}{\partial\mathbf{r}_i} \simeq \frac{1}{l_0^4}[-4(\mathbf{l}_i - \mathbf{l}_{i-1})], \tag{A5b}$$

$$\frac{\partial\kappa_{i+1}^2}{\partial\mathbf{r}_i} \simeq \frac{1}{l_0^4}[2(\mathbf{l}_{i+1} - \mathbf{l}_i)], \tag{A5c}$$

and $(\partial\kappa_j^2/\partial\mathbf{r}_i) = 0$ if $|i-j| > 1$. We obtain, finally,

$$\mathbf{f}_i^{(b)} = \frac{B}{l_0^3}[-\mathbf{l}_{i-2} + 3\mathbf{l}_{i-1} - 3\mathbf{l}_i + \mathbf{l}_{i+1}] \tag{A6}$$

$$= \frac{B}{l_0^3}[\mathbf{r}_{i-2} - 4\mathbf{r}_{i-1} + 6\mathbf{r}_i - 4\mathbf{r}_{i+1} + \mathbf{r}_{i+2}], \tag{A7}$$

for $N-3 \leqslant i \leqslant 2$. Expressions of the forces for $i < 2$ and $i > N-3$ are obtained by noticing that the summation in (A3) is for $i' = 1$ to $i' = N-2$,

$$\mathbf{f}_0^{(b)} = -\frac{B}{l_0^3}[\mathbf{r}_0 - 2\mathbf{r}_1 + \mathbf{r}_2], \tag{A8a}$$

$$\mathbf{f}_1^{(b)} = -\frac{B}{l_0^3}[-2\mathbf{r}_0 + 5\mathbf{r}_1 - 4\mathbf{r}_2 + \mathbf{r}_3], \tag{A8b}$$

$$\mathbf{f}_{N-2}^{(b)} = -\frac{B}{l_0^3}[\mathbf{r}_{N-4} - 4\mathbf{r}_{N-3} + 5\mathbf{r}_{N-2} - 2\mathbf{r}_{N-1}], \tag{A8c}$$

$$\mathbf{f}_{N-1}^{(b)} = -\frac{B}{l_0^3}[\mathbf{r}_{N-3} - 2\mathbf{r}_{N-2} + \mathbf{r}_{N-1}]. \tag{A8d}$$

2. Twist moment and forces

The twist energy of the discrete rod is

$$E^{(t)} = \frac{C}{2\,l_0}\sum_{i=1}^{i=N-2}(\theta_i - \theta_{i-1} + l_0\,\tau_{s,i})^2, \tag{A9}$$

where $\tau_{s,i}$ is the torsion of the center line at node i, and $(\theta_i - \theta_{i-1})/l_0$ is the internal twist. The torsion τ_s of the center line is obtained from Frenet-Serret equations as $\tau_s = (d\mathbf{N}/ds)\cdot\mathbf{B}$, where $(\mathbf{T},\mathbf{N},\mathbf{B})$ are the tangent, normal, and binormal vectors of the center line of the fiber. They are obtained by multiple differentiation of tangent vector $\mathbf{e}_i$, with appropriate interpolations depending upon if the derivatives are evaluated at the nodes or at the cylinder,

$$\mathbf{m}^{(t)}_{i-1;i} = \frac{C}{l_0}(\theta_i - \theta_{i-1} + l_0\,\tau_{s,i})\mathbf{e}_{i-1}. \tag{A10}$$

Taking into account the torque acting from the segment $(i+1;i+2)$ on the segment $(i;i+1)$, the total elastic twist torque acting on the segment $(i;i+1)$ is

$$\mathbf{m}^{(t)}_i = \frac{C}{l_0}[(\theta_{i+1} - \theta_i + l_0\,\tau_{s,i+1})\,\mathbf{e}_{i+1} - (\theta_i - \theta_{i-1} - l_0\,\tau_{s,i})\,\mathbf{e}_{i-1}]. \tag{A11}$$

This torque is split into two components. The axial (colinear to $\mathbf{e}_i$) component is

$$m^{(t)}_i = \mathbf{m}^{(t)}_i\cdot\mathbf{e}_i, \tag{A12}$$

whereas the remaining perpendicular component $\mathbf{m}^{(t)}_i - m^{(t)}_i\mathbf{e}_i$ is written as a system of two points forces $\mathbf{f}^{(t)}_i$ and $\mathbf{f}^{(t)}_{i+1}$ acting at points i and $i+1$ such that

$$\mathbf{f}^{(t)}_i + \mathbf{f}^{(t)}_{i+1} = 0, \tag{A13a}$$

$$(\mathbf{r}_{i+1} - \mathbf{r}_i)\times\mathbf{f}^{(t)}_{i+1} = \mathbf{m}^{(t)}_i - m^{(t)}_i\mathbf{e}_i, \tag{A13b}$$

$$\mathbf{f}^{(t)}_i\cdot\mathbf{e}_i = 0. \tag{A13c}$$

Equation (A13a) ensures that the system of two point forces is a torque, Eq. (A13b) assigns the moment, and Eq. (A13c) ensures that those forces do not stretch the rod. Using $(\mathbf{r}_{i+1} - \mathbf{r}_i) = l_i\mathbf{e}_i$, we finally obtain the two forces acting on the nodes,

$$\mathbf{f}^{(t)}_{i+1} = -\mathbf{f}^{(t)}_i = (\mathbf{m}^{(t)}_i/l_i)\times\mathbf{e}_i. \tag{A14}$$

3. Contact forces distribution

Let us take a contact force $\mathbf{f}^{(c)}$ acting at point $\mathbf{r}_C$. We are looking for two point forces $\mathbf{f}^{(c)}_i$ ($\mathbf{f}^{(c)}_{i+1}$) acting at point $\mathbf{r}_i$ ($\mathbf{r}_{i+1}$) and a moment $m_i\mathbf{e}_i$ such that

$$\mathbf{f}^{(c)}_i + \mathbf{f}^{(c)}_{i+1} = \mathbf{f}^{(c)}, \tag{A15a}$$

$$(\mathbf{r}_{i+1} - \mathbf{r}_i)\times\mathbf{f}^{(c)}_{i+1} + m^{(c)}_i\mathbf{e}_i = (\mathbf{r}_C - \mathbf{r}_i)\times\mathbf{f}^{(c)}. \tag{A15b}$$

The scalar product of Eq. (A15b) with $\mathbf{e}_i$ gives

$$m^{(c)}_i = [(\mathbf{r}_C - \mathbf{r}_i)\times\mathbf{f}^{(c)}]\cdot\mathbf{e}_i, \tag{A16}$$

and the cross product of Eq. (A15b) with $\mathbf{e}_i$ gives

$$l_i\mathbf{f}^{(c)}_{i+1} - l_i\big[\mathbf{f}^{(c)}_{i+1}\cdot\mathbf{e}_i\big]\mathbf{e}_i = \mathbf{f}^{(c)}[\mathbf{e}_i\cdot(\mathbf{r}_C - \mathbf{r}_i)] - (\mathbf{r}_C - \mathbf{r}_i)[\mathbf{e}_i\cdot\mathbf{f}^{(c)}]. \tag{A17}$$

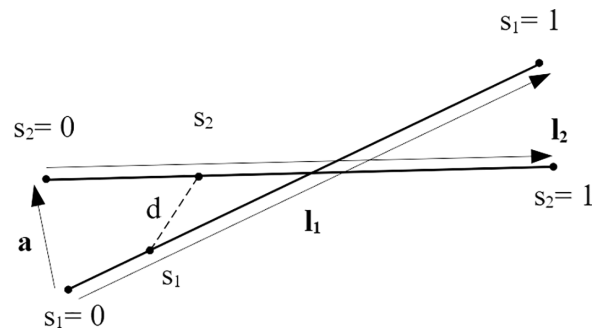

FIG. 11. Distance between two points located on two segments of the line.

Defining the parallel and perpendicular components of a force $\mathbf{f}$ with respect to the cylinder axis as

$$\mathbf{f}^{\parallel} = [\mathbf{f}\cdot\mathbf{e}_i]\mathbf{e}_i, \tag{A18a}$$

$$\mathbf{f}^{\perp} = \mathbf{f} - \mathbf{f}^{\parallel}, \tag{A18b}$$

we obtain

$$\mathbf{f}^{(c),\perp}_{i+1} = s_i\mathbf{f}^{(c),\perp} - \frac{R}{l_i}f^{(c),\parallel}\mathbf{n}. \tag{A19}$$

Equation (A19) determines only the components of $\mathbf{f}^{(c)}_{i+1}$ which are perpendicular to the axis. The parallel component of $\mathbf{f}^{(c)}_{i+1}$ is obtained in the following way. Consider the cylinder of length l_i made of an elastic material, and let k be the stiffness of the corresponding compressing spring. This cylinder may be viewed as the reunion of one cylinder of length s_il_i with stiffness k/s_i, and one cylinder of length $(1-s_i)l_i$ with stiffness $k/(1-s_i)$. Let a force $\mathbf{f}^{(c),\parallel}$ be applied at the junction between the cylinders. This force moves the junction on a distance $\delta = \|\mathbf{f}^{(c),\parallel}\|/[k/s_i + k/(1-s_i)]$. This displacement deforms the part of length $(1-s_i)l_i$ and generates a force $f^{(c),\parallel}_{i+1} = [k/s_i]\delta = s_if^{(c),\parallel}$ on this spring. Inserting this equation in Eq. (A19), we finally obtain

$$\mathbf{f}^{(c)}_{i+1} = s_i\mathbf{f}^{(c)} - \frac{R}{l_i}[f^{(c)}\cdot\mathbf{e}_i]\mathbf{n}. \tag{A20}$$

4. Distance

We consider two segments 1 and 2, whose axes are drawn in Fig. 11. On each axis are located an abscissa $s = 0$, a sphere of rayon r, and a segment of cylinder of radius r for $0\leqslant s\leqslant 1$. The distance between the two points at abscissa s_1 and s_2 is

$$d^2(s_1,s_2) = (\mathbf{a} + s_1\,\mathbf{l}_1 + s_2\,\mathbf{l}_2)^2. \tag{A21}$$

The distance is minimal for s_1^* and s_2^*, which verifies

$$\left(\frac{\partial d^2(s_1,s_2)}{\partial s_1}\right)(s_1^*,s_2^*) = \left(\frac{\partial d^2(s_1,s_2)}{\partial s_1}\right)(s_1^*,s_2^*) = 0. \tag{A22}$$

Equation (A22) is solved to obtain (s_1^*,s_2^*), and the minimal distance $d(s_1^*,s_2^*)$ is obtained. If $d(s_1^*,s_2^*) < 2r$, with

$0 \leqslant s_1^* \leqslant 1$ and $0 \leqslant s_2^* \leqslant 1$, the contact is found between the two cylinders.

If not, the contact is checked between the sphere located at $s_1 = 0$ and cylinder 2. For this, the minimal distance is obtained for s_2^*, verifying

$$\left(\frac{\partial d^2(0, s_2)}{\partial s_2}\right)(0, s_2^*) = 0. \tag{A23}$$

Equation (A23) is solved to obtain s_2^*, and the minimal distance $d(0, s_2^*)$ is obtained. If $d(0, s_2^*) < 2r$, with $0 \leqslant s_2^* \leqslant 1$, the contact is found between the sphere (1) and the cylinder (2).

The contact between sphere (2) and cylinder (1) is searched in a similar way. If not, we check for a contact between the two spheres.

[1] B. Vigolo, A. Pénicaud, C. Coulon, C. Sauder, R. Pailler, C. Journet, P. Bernier, and P. Poulin, Macroscopic fibers and ribbons of oriented carbon nanotubes, Science **290**, 1331 (2000).

[2] A. Frenot and I. S. Chronakis, Polymer nanofibers assembled by electrospinning, Curr. Opin. Colloid Interface Sci. **8**, 64 (2003).

[3] S. Toll, Packing mechanics of fiber reinforcements, Polym. Eng. Sci. **38**, 1337 (1998).

[4] V. Negi and R. C. Picu, Mechanical behavior of nonwoven noncrosslinked fibrous mats with adhesion and friction, Soft Matter **15**, 5951 (2019).

[5] N. Pan, Exploring the significance of structural hierarchy in material systems—A review, Appl. Phys. Rev. **1**, 021302 (2014).

[6] P. B. Warren, R. C. Ball, and R. E. Goldstein, Why Clothes don't Fall Apart: Tension Transmission in Staple Yarns, Phys. Rev. Lett. **120**, 158001 (2018).

[7] A. Seguin and J. Crassous, Twist-Controlled Force Amplification and Spinning Tension Transition in Yarn, Phys. Rev. Lett. **128**, 078002 (2022).

[8] J. Bohr and K. Olsen, The ancient art of laying rope, Europhys. Lett. **93**, 60004 (2011).

[9] J. W. S. Hearle, P. Grosberg, and S. Backer, *Structural Mechanics of Fibers, Yarns, and Fabrics* (Wiley, New York, 1969).

[10] S. Poincloux, M. Adda-Bedia, and F. Lechenault, Geometry and Elasticity of a Knitted Fabric, Phys. Rev. X **8**, 021075 (2018).

[11] G. Verhille, S. Moulinet, N. Vandenberghe, M. Adda-Bedia, and P. Le Gal, Structure and mechanics of *aegagropilae* fiber network, Proc. Natl. Acad. Sci. USA **114**, 4607 (2017).

[12] I. Andrade-Silva, T. Godefroy, O. Pouliquen, and J. Marthelot, Cohesion of bird nests, EPJ Web Conf. **249**, 06014 (2021).

[13] N. Weiner, Y. Bhosale, M. Gazzola, and H. King, Mechanics of randomly packed filaments—The "bird nest" as metamaterial, J. Appl. Phys. **127**, 050902 (2020).

[14] B. F. Bayman, Theory of hitches, Am. J. Phys. **45**, 185 (1977).

[15] M. K. Jawed, P. Dieleman, B. Audoly, and P. M. Reis, Untangling the Mechanics and Topology in the Frictional Response of Long Overhand Elastic Knots, Phys. Rev. Lett. **115**, 118302 (2015).

[16] B. Audoly, N. Clauvelin, and S. Neukirch, Elastic Knots, Phys. Rev. Lett. **99**, 164301 (2007).

[17] N. Clauvelin, B. Audoly, and S. Neukirch, Matched asymptotic expansions for twisted elastic knots: a self-contact problem with nontrivial contact topology, J. Mech. Phys. Solids **57**, 1623 (2009).

[18] P. Grandgeorge, C. Baek, H. Singh, P. Johanns, T. G. Sano, A. Flynn, J. H. Maddocks, and P. M. Reis, Mechanics of two filaments in tight orthogonal contact, Proc. Natl. Acad. Sci. USA **118**, e2021684118 (2021).

[19] P. Johanns, P. Grandgeorge, C. Baek, T. G. Sano, J. H. Maddocks, and P. M. Reis, The shapes of physical trefoil knots, Extreme Mech. Lett. **43**, 101172 (2021).

[20] C. Baek, P. Johanns, T. G. Sano, P. Grandgeorge, and P. M. Reis, Finite element modeling of tight elastic knots, J. Appl. Mech. **88**, 024501 (2020).

[21] H. Tangri, Y. Guo, and J. S. Curtis, Packing of cylindrical particles: Dem simulations and experimental measurements, Powder Technol. **317**, 72 (2017).

[22] P. Langston, A. Kennedy, and H. Constantin, Discrete element modeling of flexible fibre packing, Comput. Mater. Sci. **96**, 108 (2015).

[23] D. Dumont, M. Houze, P. Rambach, T. Salez, S. Patinet, and P. Damman, Emergent Strain Stiffening in Interlocked Granular Chains, Phys. Rev. Lett. **120**, 088001 (2018).

[24] M. Bergou, M. Wardetzky, S. Robinson, B. Audoly, and E. Grinspun, Discrete elastic rods, ACM Transact. Graph. **27**, 1 (2008).

[25] D. Durville, Simulation of the mechanical behaviour of woven fabrics at the scale of fibers, Intl. J. Mater. Form. **3**, 1241 (2010).

[26] D. Durville, Contact-friction modeling within elastic beam assemblies: An application to knot tightening, Comput. Mech. **49**, 687 (2012).

[27] F. Bertails-Descoubes, F. Cadoux, G. Daviet, and V. Acary, A nonsmooth Newton solver for capturing exact Coulomb friction in fiber assemblies, ACM Trans. Graph. **30**, 1 (2011).

[28] J. J. Moreau, Indetermination due to dry friction in multibody dynamics, in *European Congress on Computational Methods in Applied Sciences and Engineering*, ECCOMAS 2004 Proceedings (Jyväskylä, Finland, 2004).

[29] A. Choi, D. Tong, M. K. Jawed, and J. Joo, Implicit contact model for discrete elastic rods in knot tying, J. Appl. Mech. **88**, 051010 (2021).

[30] M. Ly, J. Jouve, L. Boissieux, and F. Bertails-Descoubes, Projective dynamics with dry frictional contact, ACM Trans. Graph. **39**, 57 (2020).

[31] B. Chareyre and P. Villard, Dynamic spar elements and discrete element methods in two dimensions for the modeling of soil-inclusion problems, J. Eng. Mech. **131**, 689 (2005).

[32] F. Bourrier, F. Kneib, B. Chareyre, and T. Fourcaud, Discrete modeling of granular soils reinforcement by plant roots, Ecol. Eng. **61**, 646 (2013).

[33] A. Effeindzourou, B. Chareyre, K. Thoeni, A. Giacomini, and F. Kneib, Modelling of deformable structures in the general framework of the discrete element method, Geotextiles Geomembranes **44**, 143 (2016).

[34] D. Kunhappan, B. Harthong, B. Chareyre, G. Balarac, and P. J. J. Dumont, Numerical modeling of high aspect ratio flexible fibers in inertial flows, Phys. Fluids **29**, 093302 (2017).

[35] A. E. H. Love, *A Treatise on the Mathematical Theory of Elasticity*, 3rd ed. (Cambridge University Press, Cambridge, 1920).

[36] J. Langer and D. A. Singer, Lagrangian aspects of the kirchhoff elastic rod, SIAM Rev. **38**, 605 (1996).

[37] G. H. M. van der Heijden and J. M. T. Thompson, Helical and localised buckling in twisted rods: A unified analysis of the symmetric case, Nonlinear Dyn. **21**, 71 (2000).

[38] P. A. Cundall and O. D. L. Strack, A discrete numerical model for granular assemblies, Géotechnique **29**, 47 (1979).

[39] S. Timoshenko and J. N. Goodier, *Theory of Elasticity*, 3rd ed. (McGraw-Hill, New York, 1970).

[40] D. Frenkel and B. Smit, Molecular dynamics simulations, in *Understanding Molecular Simulation*, 2nd ed., edited by D. Frenkel and B. Smit (Academic Press, San Diego, 2002), Chap. 4, pp. 63–107.

[41] B. Muth, M.-K. Müller, P. Eberhard, and S. Luding, Collision detection and administration methods for many particles with different sizes, in *Discrete Element Methods, DEM 07*, edited by P. Cleary (Minerals Engineering Int., 2007), pp. 1–18.

[42] K. E. Bisshopp and D. C. Drucker, Large deflection of cantilever beams, Quart. Appl. Math. **3**, 272 (1945).

[43] J. M. Gere and S. P. Timoshenko, *Theory of Elastic Stability Elasticity*, 2nd ed. (Dover, Mineola, NY, 2009).

[44] J. H. Jung, N. Pan, and T. J. Kang, Capstan equation including bending rigidity and non-linear frictional behavior, Mechanism Mach. Theor. **43**, 661 (2008).